The Peculiar X-ray Transient Swift J0840.7−3516: an Unusual Low Mass X-ray Binary or a Tidal Disruption Event?

Megumi Shidatsu,[1] Wataru Iwakiri,[2] Hitoshi Negoro,[3] Tatehiro Mihara,[4] Yoshihiro Ueda,[5] Nobuyuki Kawai,[6] Satoshi Nakahira,[7] Jamie A. Kennea,[8] Phil A. Evans,[9] Keith C. Gendreau,[10] Teruaki Enoto,[11] and Francesco Tombesi[12, 13, 14, 15]

[1]*Department of Physics, Ehime University, 2-5, Bunkyocho, Matsuyama, Ehime 790-8577, Japan*
[2]*Department of Physics, Faculty of Science and Engineering, Chuo University, 1-13-27 Kasuga, Bunkyo-ku, Tokyo 112-8551, Japan*
[3]*Department of Physics, Nihon University, 1-8-14 Kanda-Surugadai, Chiyoda-ku, Tokyo 101-8308, Japan*
[4]*High Energy Astrophysics Laboratory, RIKEN, 2-1 Hirosawa, Wako, Saitama 351-0198, Japan*
[5]*Department of Astronomy, Kyoto University, Kitashirakawa-Oiwake-cho, Sakyo-ku, Kyoto, Kyoto 606-8502, Japan*
[6]*Department of Physics, Tokyo Institute of Technology, 2-12-1 Ookayama, Meguro-ku, Tokyo 152-8551, Japan*
[7]*High Energy Astrophysics Laboratory, RIKEN, 2-1, Hirosawa, Wako, Saitama 351-0198, Japan*
[8]*Department of Astronomy and Astrophysics, Pennsylvania State University, University Park, PA 16802, USA*
[9]*Department of Physics and Astronomy, University of Leicester, Leicester LEI 7RH, UK*
[10]*Astrophysics Science Division, NASA Goddard Space Flight Center, Greenbelt, MD 20771, USA*
[11]*Extreme Natural Phenomena RIKEN Hakubi Research Team, RIKEN Cluster for Pioneering Research, 2-1 Hirosawa, Wako, Saitama 351-0198, Japan*
[12]*Department of Astronomy, University of Maryland, College Park, MD 20742, USA*
[13]*NASA/Goddard Space Flight Center, Code 662, Greenbelt, MD 20771, USA*
[14]*Department of Physics, Tor Vergata University of Rome, Via della Ricerca Scientifica 1, I-00133 Rome, Italy*
[15]*INAF Astronomical Observatory of Rome, Via Frascati 33, I-00078 Monte Porzio Catone, Italy*

ABSTRACT

We report on the X-ray properties of the new transient Swift J0840.7−3516, discovered with *Swift*/BAT in 2020 February, using extensive data of *Swift*, MAXI, NICER, and *NuSTAR*. The source flux increased for $\sim 10^3$ s after the discovery, decayed rapidly over ~ 5 orders of magnitude in 5 days, and then remained almost constant over 9 months. Large-amplitude short-term variations on time scales of 1–10^4 s were observed throughout the decay. In the initial flux rise, the source showed a hard power-law shaped spectrum with a photon index of ~ 1.0 extending up to ~ 30 keV, above which an exponential cutoff was present. The photon index increased in the following rapid decay and became ~ 2 at the end of the decay. A spectral absorption feature at 3–4 keV was detected in the decay. It is not straightforward to explain all the observed properties by any known class of X-ray sources. We discuss the possible nature of the source, including a Galactic low mass X-ray binary with multiple extreme properties and a tidal disruption event by a supermassive black hole or a Galactic neutron star.

Keywords: X-rays: individual (Swift J0840.7−3516)

1. INTRODUCTION

Observations of X-ray transients have provided valuable opportunities to study a huge variety of Galactic and extragalactic variable sources, from stellar objects including flaring stars, cataclysmic variables (CVs), X-ray binaries, and Gamma-ray bursts (GRBs), to su-

permassive black holes, including active galactic nuclei (AGN) and tidal disruption events (TDEs) of stars. In particular, the combination of all-sky monitoring and follow-up observations have deepened our knowledge of their behavior both in early and late phases after their emergence, and helped us to achieve critical information of their nature and physical mechanisms of energetic transient phenomena.

Swift J0840.7−3516 (also known as GRB 200205A) was discovered with *the Neil Gehrels Swift Obser-*
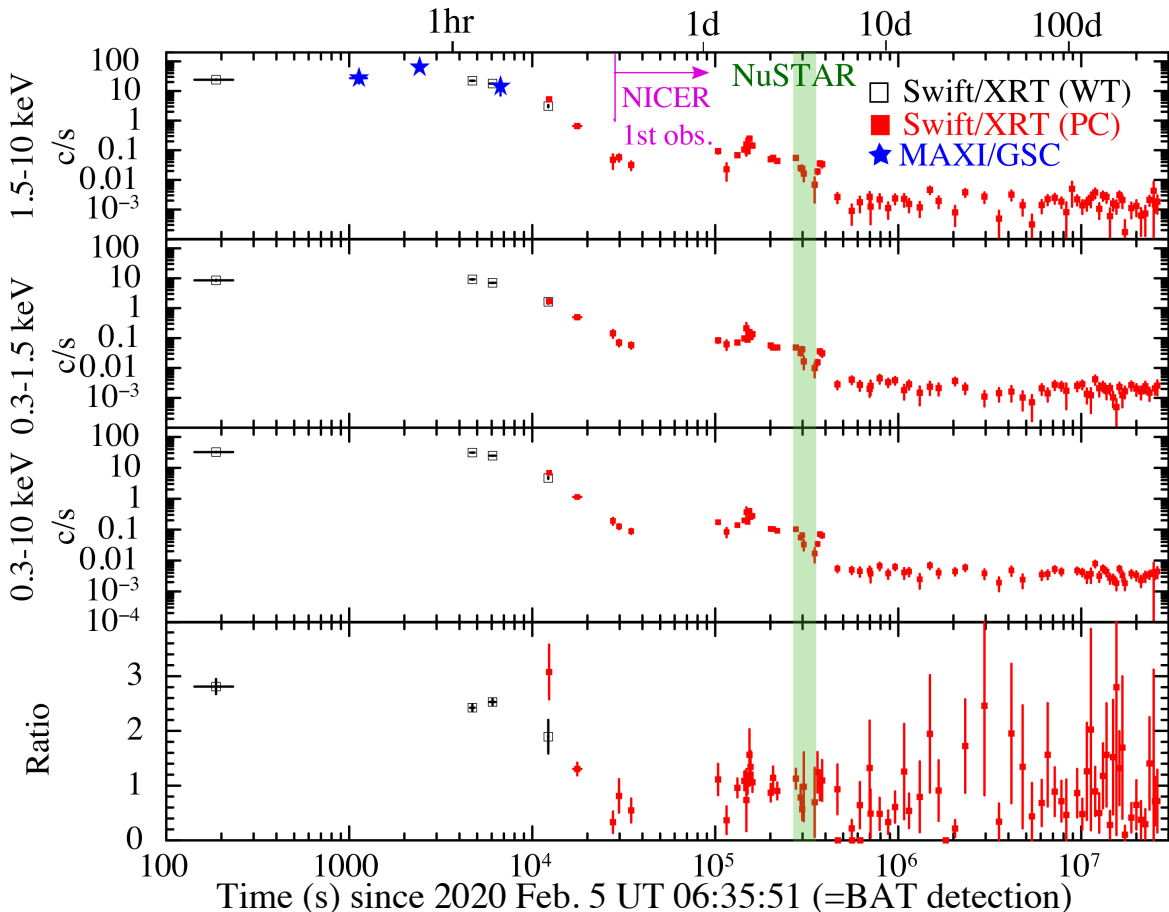
Corresponding author: Megumi Shidatsu
shidatsu.megumi.wr@ehime-u.ac.jp

Figure 1. *Swift*/XRT light curves in 1.5–10 keV, 0.3–1.5 keV, and 0.3–10 keV, and the hardness ratio between 1.5–10 keV and 0.3–1.5 keV, from top to bottom. The black open and red filled squares represent the Windowed-Timing (WT) mode and the Photon-Counting (PC) mode data, respectively. They are binned in each snapshot before 4×10^5 s from the BAT detection ($T = 0$) and in each observation for the later time. Errors in the abscissa and ordinate represent the start/end times of the bin from the mean photon arrival time, and the 1σ errors of the count rates or the ratios, respectively. MAXI/GSC data are also plotted with blue stars (see 2.2 for the conversion to XRT count rates).

vatory (*Swift*; Gehrels et al. 2004) on 2020 February 5 UT 06:35 (Evans et al. 2020; Kennea et al. 2020; Osborne et al. 2020), located at ~ 4 deg above the Galactic plane. Monitor of All-sky X-ray Image (MAXI; Matsuoka et al. 2009) nova alert system (Negoro et al. 2016) also detected the source about 20 minutes after the *Swift* detection (Niwano et al. 2020). The MAXI/Gas Slit Camera (GSC) intensity increased from ~ 70 mCrab to ~ 210 mCrab in the 2–10 keV band from the first to second scan after the *Swift* detection, and then rapidly decreased to ~ 30 mCrab in the third scan. Follow-up X-ray observations has been made with *Swift* and the Neutron star Interior Composition ExploreR (NICER; Gendreau et al. 2016) 59 and 16 times (as of 2020 December 10), respectively, and once with the Nuclear Spectroscopic Telescope Array (*NuSTAR*; Harrison et al. 2013) in 2020 February 8–9. A possible periodicity of 8.96 s was reported by using the

Swift/XRT data (Kennea et al. 2020), but in following NICER observations no periodic variations were significantly detected (Iwakiri et al. 2020).

Optical and UV counterparts were found in photometric observations (Lipunov et al. 2020; Melandri et al. 2020; Malesani et al. 2020; Mazaeva & IKI-FuN followFUp Collaboration 2020). Malesani et al. (2020) suggested that the source may be a Galactic source rather than a GRB because of the location and an unusually high optical/gamma-ray brightness ratio at early phases. No radio counterpart has been found so far; Borghese et al. (2020) posed a 3σ upper limit of 18 μJy at 7.25 GHz using Australia Telescope Compact Array (ATCA) on 2020 February 11.

Despite the intensive follow-up observations, the nature of Swift J0840.7−3516 is still unknown. In this article, we analyze X-ray data of the source obtained with

Swift, MAXI, NICER, and *NuSTAR* to understand its nature and radiation processes. We utilized HEAsoft version 6.26.1 for data reduction and analysis. Errors represent 90% confidence ranges of single parameters unless otherwise specified.
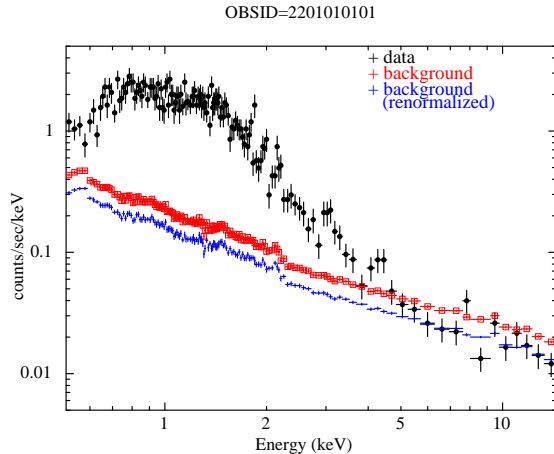

OBSID=2201010101

Figure 2. (Black filled circles) time-averaged, folded spectrum produced from the first NICER observation (OBSID=2201010101). Background is not subtracted. (Red open squares) background spectrum generated with `nibackgen3C50`. (Blue crosses) the same background spectrum renormalized so that its 10–15 keV count rate equals to that of the data.

2. OBSERVATION AND DATA REDUCTION

2.1. *Swift*

Since the first BAT detection at February 5 UT 06:35, *Swift* observed the source almost every day in February and about once a week from the beginning of March to the end of November, with exposure times of 0.1–5 ks. We used all XRT data of the 59 observations. Figure 1 shows the *Swift*/XRT light curves and hardness ratio for the entire period, obtained via the web interface provided by the *Swift* team[1] (Evans et al. 2007, 2009), in which we used the latest CALDB (version 2019 September 10) when this source was first observed with *Swift*. The same interface was used to retrieve XRT spectra. We created time-averaged spectra for the individual observations until February 9. An exception is the second observation (OBSID=00954304001) performed in February 5 UT 07-16, which was divided into each snapshot (i.e., each continuous exposure) interval because of strong variations, although the last three intervals in UT 14-16 were merged due to low statistics. We combined the data for every ∼40 days from Febru-

ary 10 to June 14, and merged all the data from June 15 and later, to improve statistics of the spectra after the decay.

A time-averaged hard X-ray spectrum was also made from the BAT event-mode data taken at the first detection on February 5 (OBSID=00954304000). The BAT data were downloaded from HEASARC archive[2] and processed with the script `batgrbproduct` included in HEAsoft, referring to the *Swift*/BAT Calibration Database (CALDB) released on 2017 October 16. We adopted the default binning (binned in every 2 keV) to produce the spectrum.

2.2. *MAXI*

MAXI/GSC detected the source ∼20 minutes after the BAT detection and the subsequent two scans. We retrieved the GSC data in these individual scans via the on-demand system[3]. The GSC data are plotted in the top panel of Fig. 1, together with the XRT data. They were converted to the XRT count rates in 1.5–10 keV through the HEASARC online tool WebPIMMS (Mukai 1993)[4], using the best-fit parameters of the absorbed power-law model obtained from the time-averaged spectra in the corresponding scans (see Section 3.3.1). As noticed in the figure, MAXI uniquely observed the source around the flux peak of Swift J0840.7−3516.

2.3. *NICER*

NICER started the first observation ∼8 hours after the BAT detection, and revisited the source every 1–few days until February 27, with exposure times of 0.4–10 ks. We used all the data taken before February 9, which have sufficient statistics for spectral and timing analysis. The NICER/XTI data were downloaded from HEASARC archive. They were reprocessed with the pipeline tool `nicerl2` based on the NICER CALDB version 2020 February 2, before producing light curves and time-averaged spectra of the individual OBSIDs. The response matrix file `nixtiref20170601v001.rmf` and ancillary response file `nixtiaveonaxis20170601v003.arf` were adopted in spectral analysis. The background generator `nibackgen3C50` version 4 was utilized to produce background spectra for each observation. The estimated background level was found to be overestimated in some OBSIDs, as shown in Figure 2. To absorb the deviation, we adjusted the normalizations of the background spectra of the individual OBSIDs so that the count rates in
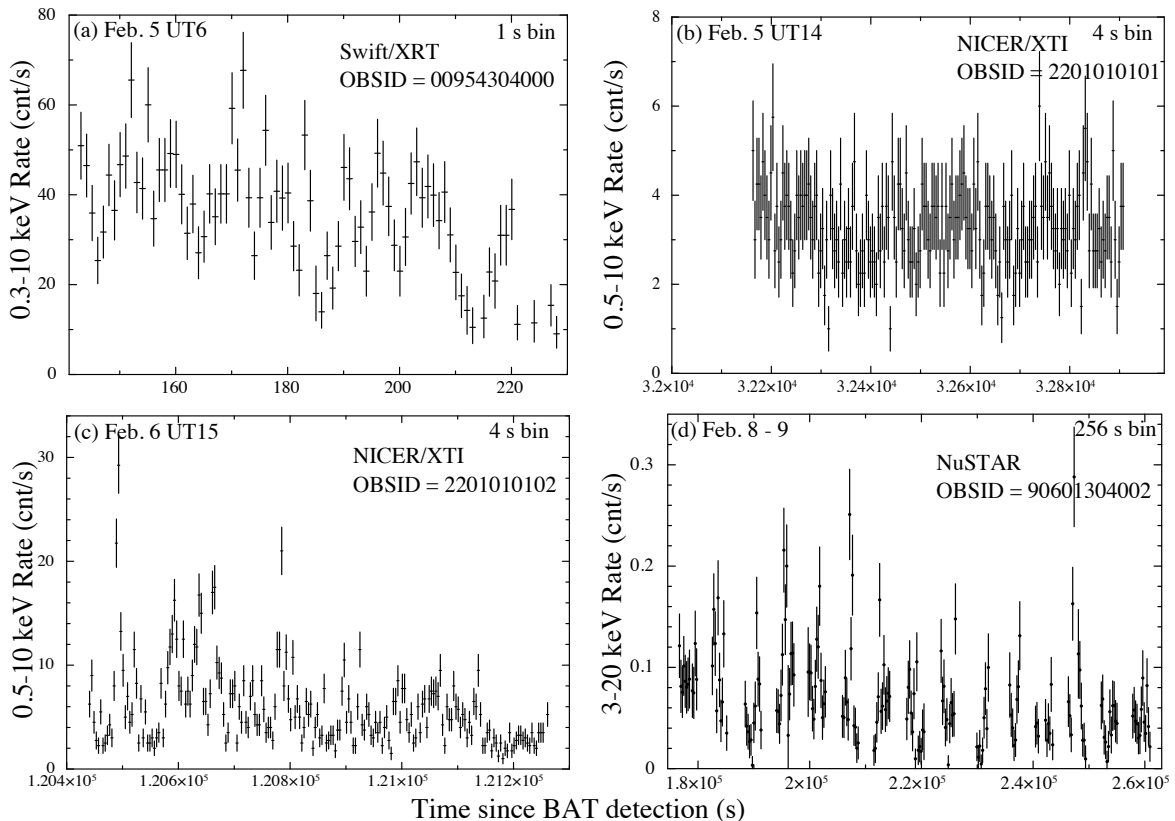

Figure 3. Short-term light curves in different periods. Note that different energy ranges are adopted for *Swift*, NICER, and *NuSTAR* (see the labels of the ordinate axes). Background component is not subtracted in the NICER light curves. For clarity, the NICER light curves only cover the first continuous scans of the observations, while the other two include the entire periods of the observations.

10–15 keV (where background counts are dominant) are equal between the actual data and the generated background spectra. The renormalization factors are within the range of 0.9–1.4. We have found that this treatment only slightly changes the results of the spectral fits in the following sections (by $< 15\%$ for the flux and $< 5\%$ for the other parameters) from those obtained by using the original background spectra and that this does not affect the conclusions of the paper.

2.4. *NuSTAR*

The *NuSTAR* observation was performed from February 8 UT 07:18 to 9 UT 06:46 with an exposure time in the normal observing mode of 42 ksec (after standard screening to produce cleaned event data was applied). The *NuSTAR* data were retrieved from the HEASARC archive and reprocessed through `nupipeline` and the latest *NuSTAR* CALDB as of 2020 February 5. *NuSTAR* light curves, the time-averaged spectrum, and its response files were created with `nuproducts`. The source and background region were defined as circular regions with a radius of 50" centered on the target position, and with a 80" radius in a blank sky area on the same chip, respectively.

3. ANALYSIS AND RESULTS

3.1. *Long-term Light Curve*

As shown in Fig. 1, the source initially increased its intensity and reached the peak at $T \sim 10^3$ s (where T is the time since the BAT trigger). It then exhibited a very rapid decay, decreasing its 1.5–10 keV intensity by ~ 5 orders of magnitude in $< 10^6$ s. In the decay, the source showed a plateau phase from $T \sim 3 \times 10^4$ s to $T \sim 1 \times 10^5$ s. In the early decline phase before the plateau, the hardness ratio, calculated by dividing the 1.5–10 and 0.3–1.5 keV count rates, rapidly decreased, indicating spectral softening. After the end of the decay at $T \sim 5 \times 10^5$ s, the source showed flat light curves in all energy ranges, with a non-periodic variation by a factor of ~ 2 (see the third panel of Fig. 1).

3.2. *Short-term Variability*

Figure 3 displays examples of short-term light curves at different periods. Strong variation on time scales of 1–10^3 s can be seen throughout the decay. The X-ray intensity varied by a factor of several to even more than one order of magnitude (see Fig. 3d), although the amplitude became somewhat weaker around the end of the
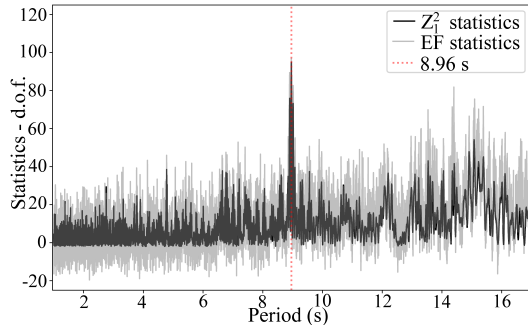
Figure 4. Periodogram of *Swift*/XRT WT-mode data taken on 2020 February 5, with an exposure time of 765 s. Analysis using Z_1^2 search (Buccheri et al. 1983) and e-folding techniques are over-plotted (black and gray, respectively). A clear peak is seen at $P = 8.96$ s (red dotted line). This represents the only dataset in which this period is detected.
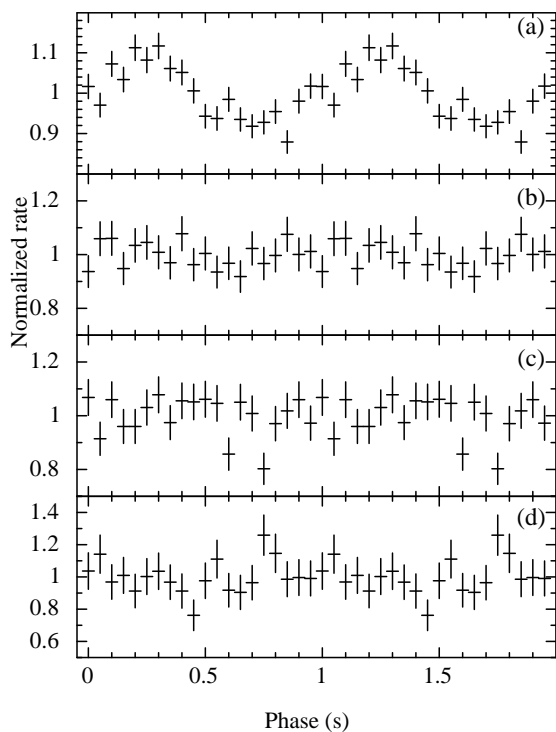

Figure 5. Light curves in Fig. 3(a)–(d) folded by 8.96 s, normalized by their averaged count rates. The *Swift*/XRT data of OBSID=00954304001 were added to (a) and the whole observation periods were used in (b)–(d).

initial decline, $T \sim 3 \times 10^4$ s (Fig. 3c). We note that the strong variability was also clearly seen in the MAXI scan around the flux peak ($T \sim 10^3$ s).

We searched for periodicity using the available *Swift*/XRT, NICER, and *NuSTAR* data, after applying barycentric correction for the target position (RA, Dec)(J2000) = ($08^h40^m40^s.84$, $-35°16'24''.8$) with the

ftool `barycorr`, based on the JPL planetary ephemeris DE-200. Adopting the Z_1^2 (Buccheri et al. 1983) and epoch-folding techniques, we found a peak at 8.96s in the periodogram of the first *Swift*/XRT WT-mode observations (OBSID=00954304000 and 00954304001; Fig. 4), which is consistent with the report by Kennea et al. (2020). The chance probability of this 8.96s period was $< 10^{-10}$ based on the Z_1^2 method. No significant periodicity was detected in the other data. In Figure 5 we plot the light curve in Fig. 3 folded by 8.96 s using the ftool `efold`.

Using the light curves, we also searched for possible Type-I X-ray bursts, which are characterized by a short rise time of $\lesssim 10$ s and a subsequent longer decay for a few ten seconds or more (e.g., Lewin et al. 1993). However, no evidence of the X-ray bursts were found in any of the *Swift*, NICER, and *NuSTAR* data. Specifically, the flare seen in the *NuSTAR* light curve (Fig. 3d) at $\sim 2.48 \times 10^5$ s from the BAT detection was found to have a ~ 200-s rise time, by using a light curve with shorter time bins, and hence is unlikely to be a Type-I X-ray burst.

3.3. Analysis of X-ray Spectrum
3.3.1. Overall Spectral Evolution

Figure 6 presents representative soft X-ray spectra obtained with the *Swift*/XRT, MAXI/GSC, and NICER/XTI at different epochs. The spectrum was hardest at the initial, brightest phase ($T \lesssim 10^4$ s), then rapidly softened, and finally became almost flat in the EF_E form. A hint of an absorption feature is seen at 3–4 keV in the *Swift* and NICER spectra taken in $T = 2 \times 10^4$–5×10^4 s (blue and magenta spectra in the Fig. 6 left panel), which we look into in Section 3.3.2.

To quantify the overall spectral behavior, we applied an absorbed power-law model to each spectrum. Throughout the spectral analysis, we used the 0.5–10 keV, 2–20 keV, and 1.0–10 keV ranges of the *Swift*, MAXI and NICER data, respectively. C-statistic (Cash 1979) was employed because many of the spectra have relatively low statistics. The `TBabs` model was adopted for the absorption component, with the solar abundance table given by Wilms et al. (2000). The equivalent hydrogen column density N_H was allowed to vary in *Swift* and NICER data, while fixed in the MAXI data at 3×10^{21} cm^{-2}, which is the Galactic column in the direction of Swift J0840.7−3516 estimated with the tool `nh` in HEAsoft. This is because MAXI is not sensitive to the soft X-rays below 2 keV and difficult to constrain N_H. We note that the free parameters obtained from the MAXI spectra remained consistent within their 90 % confidence ranges when $N_H = 0$ and 1.0×10^{22} cm^{-2}
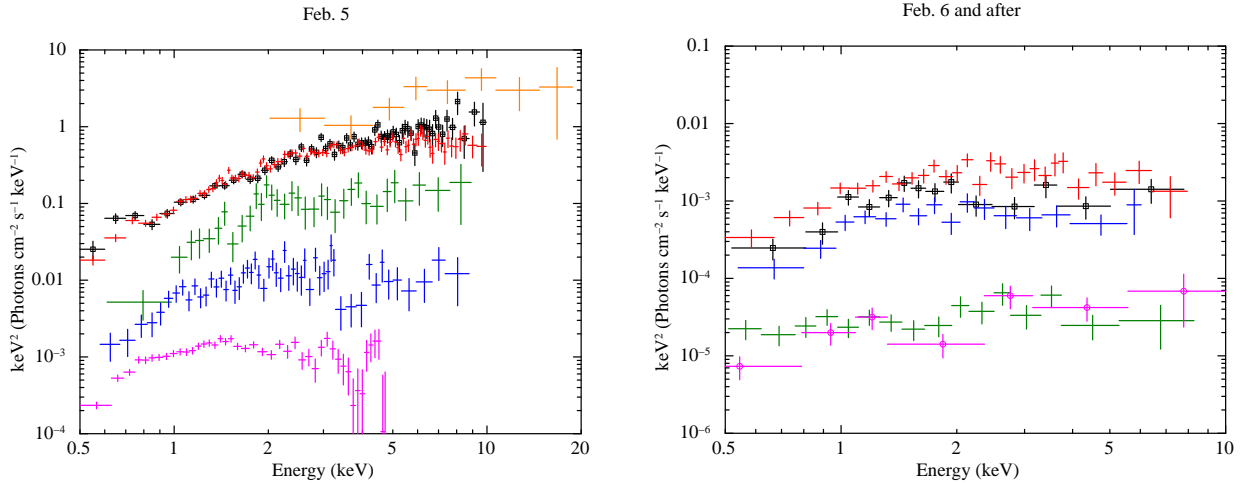
Figure 6. Representative spectra on 2020 February 5 (left) and after (right), unfolded by using a single power-law model with a photon index of 2. (Left) The data of the first *Swift*/XRT observation in $T = (1.4\text{–}2.3) \times 10^2$ s are presented with black open squares. The others are the MAXI/GSC spectrum obtained in $T = (2.3\text{–}2.5) \times 10^3$ s (orange), *Swift*/XRT spectra in $(4.5\text{–}4.8) \times 10^3$ s (red), $(1.22\text{–}1.24) \times 10^4$ s (green), and $(1.8\text{–}1.9) \times 10^4$ s (blue), and NICER/XTI spectrum in $(2\text{–}5) \times 10^4$ s (magenta), from top to bottom. (Right) *Swift*/XRT spectra obtained in $T = (1.0\text{–}1.3) \times 10^5$ s (black open squares), $(2.3\text{–}2.5) \times 10^5$ s (red), $(2.7\text{–}3.0) \times 10^5$ s (blue), and $(4\text{–}37) \times 10^5$ s (green), and $(8\text{–}11) \times 10^6$ s (magenta open circles). Note that some of the spectra were obtained by averaging multiple intermittent observations (see Fig. 1).
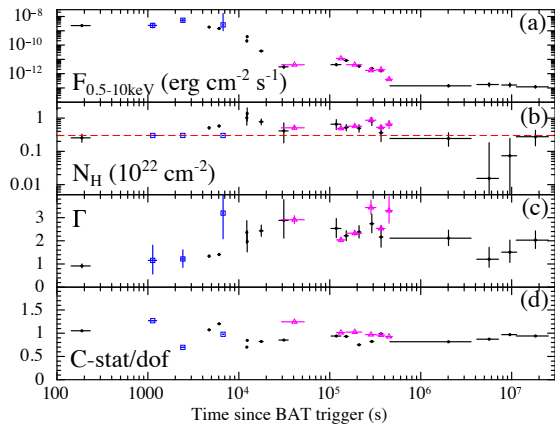

Figure 7. Time variations in the best-fit parameters of the absorbed power-law model: (a) unabsorbed 0.5–10 keV flux, (b) $N_{\rm H}$, (c) Γ, (d) C-statistic/(degree of freedom). *Swift*, MAXI, and NICER data are presented in black circles, blue squares, magenta triangles, respectively. The red dashed line in the panel (b) shows the total Galactic column ($N_{\rm H} = 3 \times 10^{21}$ cm^{-2}).

Table 1. Best-fit parameters of absorption components.

Parameter	Unit	*Swift*	NICER
(1) `TBabs*edge*powerlaw`			
$E_{\rm edge}$	keV	3.3 ± 0.1	$3.4^{+0.6}_{-0.2}$
τ		1.43 ± 0.7	$0.52^{+0.78}_{-0.51}$
C-stat/d.o.f		204/263	316/326
(2) `TBabs*(gauss+powerlaw)`			
$E_{\rm cen}$	keV	$3.7^{+0.2}_{-0.1}$	$3.9^{+0.1}_{-0.2}$
σ	keV	$0.2^{+0.2}_{-0.1}$	< 0.36
$N_{\rm gau}$ [a]		$5^{+2}_{-3} \times 10^{-4}$	$1.4^{+1.7}_{-1.1} \times 10^{-5}$
EW	keV	$0.5^{+0.3}_{-0.2}$	$0.24^{+0.29}_{-0.18}$
C-stat/d.o.f		206/262	314/325
`TBabs*powerlaw` (continuum)			
C-stat/d.o.f		276/265	319/328

[a] Absolute value of the normalization of `gauss`, defined as the total photon flux in the absorption line, in units of photons cm^{-2} s^{-1}.

were adopted. When $N_{\rm H}$ is allowed to vary, it is not constrained at all and only the lower limits of Γ and unabsorbed fluxes were obtained.

The model successfully reproduced all the spectra. Figure 7 plots the individual fit parameters in the chronological order. The spectrum until $T \sim 10^4$ s had a small photon index of $\Gamma = 1.0\text{–}1.2$. The value increased in the following rapid decline, and became $\Gamma \sim 2.0$ after the decay. During the decay, the column density was comparable with the total Galactic column, except

for the plateau phase in $T \sim 3 \times 10^4\text{–}10^5$ s, where $N_{\rm H}$ increased up to $\sim 1 \times 10^{22}$ cm^{-2}. At this phase, Γ was estimated to be a slightly larger value, $\Gamma \sim 2\text{–}3$. These behaviors may suggest variations of the intrinsic absorption, although it could be affected by the degeneracy with Γ. At late times of and after the decay, the $N_{\rm H}$ values are consistent with or slightly smaller than
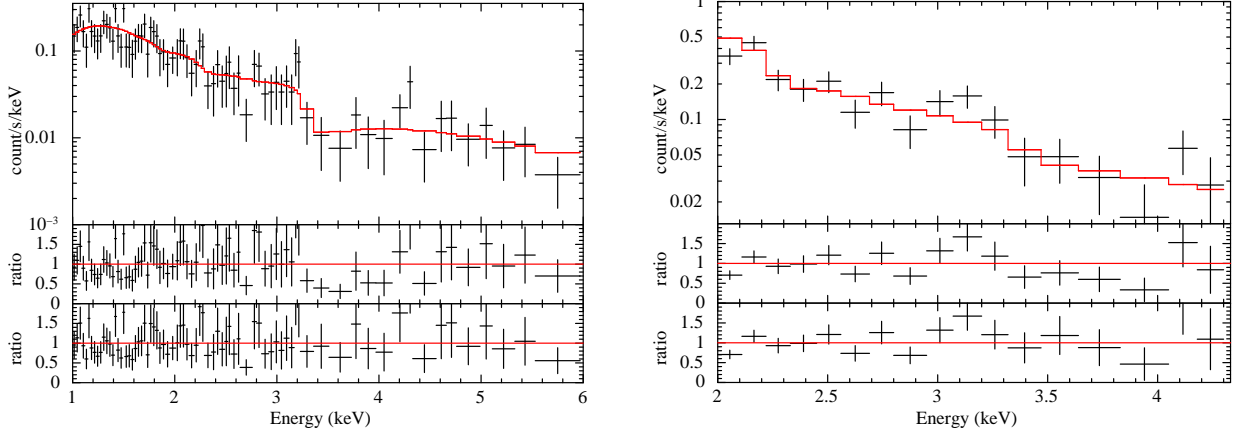
Figure 8. *Swift*/XRT (left) and NICER (right) spectra and the best-fit `TBabs*edge*powerlaw` model. The data versus model ratios for the models excluding and including `edge` are plotted in the middle and bottom panels, respectively.
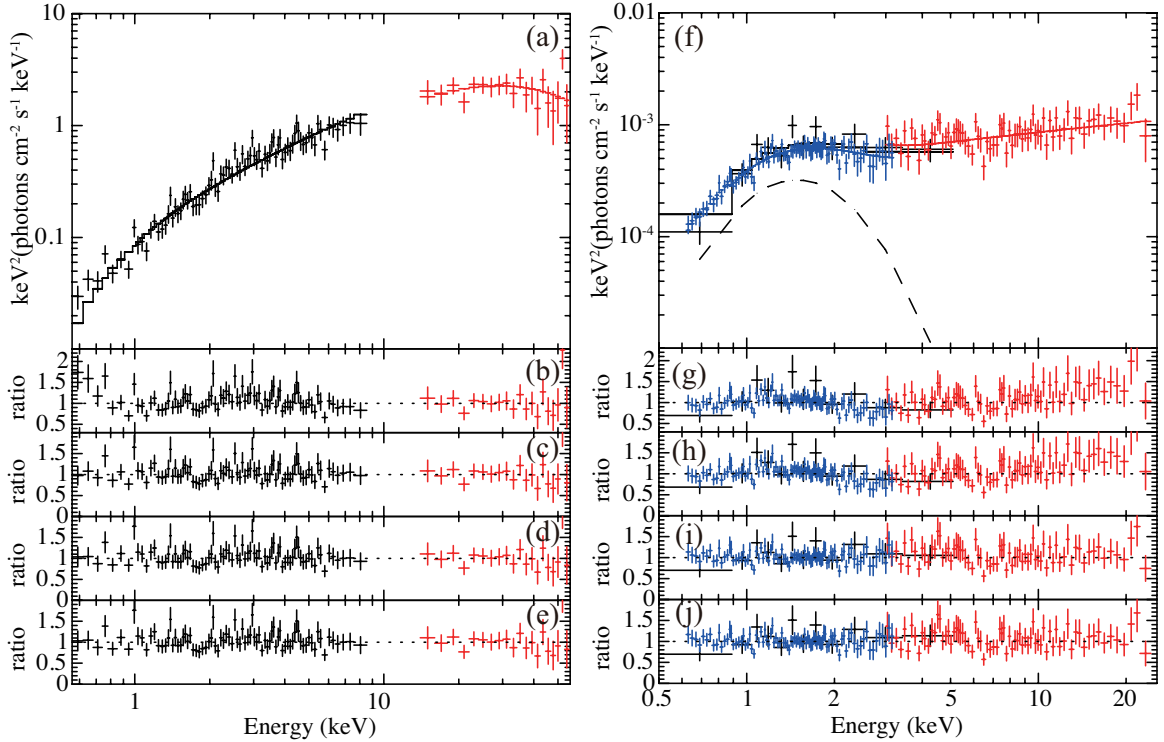

Figure 9. Wide-band X-ray spectra obtained at $T \sim 2 \times 10^2$ s (left) and $\sim 2 \times 10^5$ s (right), fitted with 4 different models. The *Swift*, NICER, and *NuSTAR* data are plotted in black, blue, and red, respectively. The best-fit `TBabs*pcfabs*powerlaw` model and `TBabs*(bbodyrad+powerlaw)` model are adopted in the panels (a) and (f), respectively. The dashed line in panel (f) presents the contribution of `bbodyrad`. The data versus model ratios for `TBabs*powerlaw` (b and g), `pcfabs*TBabs*powerlaw` (c and h), `TBabs*(bbodyrad+powerlaw)` (d and i), and `TBabs*pcfabs*powerlaw` (e and j) are also plotted.

the Galactic column, but have large uncertainties due to the low statistics.

3.3.2. *Absorption Structure*

In Fig. 6, a possible absorption feature was found at 3–4 keV in the *Swift* and NICER spectra obtained in $T = 2 \times 10^4$–5×10^4 s. To describe the profile, we tested (1) a Gaussian line model (`gauss`, with a negative nor-

malization) and (2) a simplified edge model (`edge`). The same absorbed power-law model as in Section 3.3.1 was used as the continuum model, where all the parameters were allowed to vary. We also adopted the same energy ranges of the spectra as those in that section.

The best-fit values of the `gauss` and `edge` components are listed in Table 1, and the *Swift*/XRT and NICER data and their best-fit models with `edge` are shown in

Table 2. Best-fit parameters for the wide-band spectra.

ID	$N_{\rm H}$	Γ	$E_{\rm cut}$	N^a	$kT_{\rm in}$, $kT_{\rm bb}$	$R_{\rm in}$, $R_{\rm bb}{}^b$	$N_{\rm H}^{\rm pcf}$	$C_{\rm v}{}^c$	$F_{\rm X}$	χ^2/dof
	10^{21} cm^{-2}		keV		keV	km	10^{21} cm^{-2}		erg s^{-1} cm^{-2}	
TBabs*cutoffpl										
SP1	2.4 ± 0.1	0.8 ± 0.1	24^{+7}_{-5}	0.13 ± 0.02	–	–	–	–	9×10^{-9}	119/99
SP2	2.5 ± 0.3	1.98 ± 0.09	> 196	$(7 \pm 1) \times 10^{-4}$	–	–	–	–	5×10^{-12}	204/172
TBabs*pcfabs*cutoffpl										
SP1	< 1.8	$1.2^{+0.3}_{-0.1}$	36^{+30}_{-9}	$0.24^{+0.12}_{-0.04}$	–	–	17^{+13}_{-5}	$0.7^{+0.04}_{-0.15}$	8×10^{-9}	96/97
SP2	2.6 ± 0.2	2.0 ± 0.1	> 193	$(7 \pm 1) \times 10^{-4}$	–	–	< 0.25	$-^e$	5×10^{-12}	203/170
TBabs*(bbodyrad+cutoffpl)										
SP1	6.8 ± 0.2	1.0 ± 0.2	30^{+14}_{-8}	$0.19^{+0.04}_{-0.03}$	$0.07^{+0.02}_{-0.01}$	$6^{+12}_{-4} \times 10^3$	–	–	8×10^{-9}	97/97
SP2	2.1 ± 0.5	$1.7^{+0.1}_{-0.2}$	> 49	$(4 \pm 1) \times 10^{-4}$	0.33 ± 0.05	$2.0^{+0.8}_{-0.5}$	–	–	6×10^{-12}	150/170
TBabs*(diskbb+cutoffpl)										
SP1	6.7 ± 0.2	1.0 ± 0.2	31^{14}_{-8}	$0.19^{+0.04}_{-0.03}$	0.08 ± 0.02	$8^{+19}_{-6} \times 10^3$	–	–	8×10^{-9}	97/97
SP2	$2.6^{+0.5}_{-0.4}$	$1.7^{+0.1}_{-0.3}$	> 33	$(3 \pm 1) \times 10^{-4}$	0.5 ± 0.1	$1.4^{+0.7}_{-0.4}$	–	–	6×10^{-12}	150/170

[a] Normalization of cutoffpl, defined as the photon flux in units of photons keV^{-1} cm^{-2} s^{-1} at 1 keV.

[b] $D = 8$ kpc and $i = 60°$ (for diskbb) were assumed.

[c] Covering fraction of pcfabs.

[d] Unabsorbed 1–100 keV flux.

[e] Not constrained.

Fig. 8. The quality of fit for the *Swift*/XRT spectrum was significantly improved from the case of the continuum model, whereas the improvement was not significant in the NICER data. Using the script simftest on XSPEC, we estimated the chance probability of improvement by the additional edge component as 0.001 and 0.2 (corresponding $\sim 4\sigma$ and $\sim 1\sigma$) for the *Swift* and NICER data, respectively. The two spectra gave consistent edge/line energies. The Fe K line and/or edge around 6–7 keV are most prominently seen in many X-ray sources including accreting black holes and neutron stars. Assuming the observed feature originated in the neutral Fe K-shell edge, the redshift estimated from the edge model is as $z \sim 1.1$, (see Section 4.2 for discussion).

If the feature is the neutral Fe K absorption edge of cold gas, Fe K emission or absorption lines would also be produced, depending on its geometry and temperature. We tested to add a negative/positive Gaussian component at $z = 1.1$ with a line center energy of 6.4 keV to the absorbed power-law continuum model, to consider the neutral Fe Kα absorption/emission line. The 90% upper limits of the line strengths for the *Swift* data were estimated to be 4.0×10^{-4} and 3.3×10^{-4} photons cm^{-2} s^{-1} ($\sim 1.2 \times 10^2$ eV and ~ 97 eV in the equivalent width), for the positive and negative Gaussian cases, respectively.

We also applied, to the *Swift* spectrum, the neutral Compton reflection model pexmon (Nandra et al. 2007), which accounts for both the Fe K emission lines and edge self-consistently, to test the possibility of a reflection component like those seen in X-ray binaries and AGNs. We replaced the power-law component in the original continuum model to pexmon and allowed to vary the reflection scale factor (rel_refl), which is the solid angle Ω of the reflector visible from the illuminating source, in units of 2π. The abundance of Fe and other elements was assumed to be the same as the Solar abundance, and the redshift and the cutoff energy were fixed at 1.1 and 0 keV (i.e., the high energy cutoff was not included). We tested the two cases of inclination angles: $i = 0°$ and $60°$. In both cases, the model gave somewhat better fits than the absorbed power-law model, yielding C-stat/d.o.f. $= 217/263$. We obtained only a weak upper limit of the reflection factor, $\Omega/2\pi < 2.0$ and 2.6, for $i = 0°$ and $60°$, respectively.

3.3.3. *Analysis of Wide-band Spectra*

Hard X-ray spectra with good statistics were obtained from the *Swift*/BAT observation at an early phase ($T \sim 10^2$ s) and the *NuSTAR* observation in the last part of decay ($T \sim 2 \times 10^5$ s). Combining them with the *Swift*/XRT and NICER data taken

(quasi-)simultaneously, we obtained wide-band spectra in $T \sim 2 \times 10^2$ s (Hereafter SP1) and in $T \sim 2 \times 10^5$ s (SP2), as shown in Figure 9(a) and (f), respectively. The SP1 spectrum was produced from the *Swift*/XRT and BAT data of OBSID=00954304000, and the SP2 spectrum was from the *Swift*/XRT, NICER, and *NuSTAR* data of OBSID=00954304004, 2201010105, and 90601304002, respectively. The former spectrum has a clear high-energy cutoff at ~ 30 keV, while the latter shows a flat profile extending to at least ~ 20 keV. Here, we adopted χ^2 statistics for the *Swift*/BAT spectrum, because it was already grouped by channels to have Gaussian distribution and hence C-statistics should not be used[5]. For consistency, the χ^2 statistics are applied to the *Swift*/XRT, NICER, and *NuSTAR* spectra as well. To ensure that the distribution underlying the data can be approximated by the Gaussian distribution, the *Swift*/XRT data of SP1 were binned so that at least 40 counts are included in each spectral bin. The *Swift*/XRT, NICER, and *NuSTAR* spectra in SP2 were binned to have minimum 20, 20, and 40 counts per bin, respectively.

We first fit the two spectra with an absorbed cutoff power-law model: `TBabs*cutoffpl` in the XSPEC terminology. The model versus data ratios are shown in Figure 9(b) and (g) and the best-fit parameters are listed in Table 2. Although the model fit both spectra fairly well, small residual structures remained. In Fig. 9(b) discrepancy between the data and model can be seen at lowest energies, and in Fig. 9(g), a small hump in 0.8–2 keV and an excess above ~ 10 keV are present.

Next we investigated if an additional, optically-thick thermal component or partial covering absorption can better reproduce the soft X-ray profiles. We adopted `pcfabs` as the partial covering absorption model at $z = 0$. For the thermal component, we tested a black-body component (`bbodyrad`) and a disk blackbody component (`diskbb`; Mitsuda et al. 1984). In SP1, these models significantly improved the quality of fit (Fig. 9c, d, and e), and in any of the models the χ^2 values decreased by ~ 20 with the degrees of freedom reduced by 2 (Tab. 2) from the simple absorbed cutoff power-law model. The fit quality of SP2 was not improved by adding the `pcfabs` model (Fig. 9h), but an additional thermal component (Fig. 9i and j) reduced the χ^2 value by ~ 50. We obtained a low temperature and a large radius of (disk) blackbody in SP1, while a slightly higher temperature and a much smaller radius in SP2.

---

[5] https://swift.gsfc.nasa.gov/analysis/threads/batspectrumthread.html

3.4. *Profile of Flux Decay*

To investigate the profile of the long-term flux decay, we analyzed the flux light curve in Fig. 7(a), obtained in the analysis of the soft X-ray spectra based on the absorbed power-law model (see Section 3.3.1). First, to roughly characterise the decay profile, we fitted the data points with a single power-law function in terms of the time T from the BAT detection:

$$F_{\mathrm{X}} \propto (T - T_{\mathrm{peak}})^{-\alpha}, \qquad (1)$$

where F_{X} is the unabsorbed 0.5–10 keV flux and T_{peak} is the time at the flux peak, which we assumed to be the second scan of MAXI at $T \approx 2 \times 10^3$ s. Here, we only considered the decay period from $T \approx 1 \times 10^3$ s to 2×10^4 s and ignored the initial flux rise, the final constant-flux phase, and the plateau phase in $T \approx (2$–$5) \times 10^4$ s during the decay. A decay index of $\alpha \approx 1.7$ was found to approximately reproduce the observed decay.

Next, we applied a multiply broken power-law model to the flux data over the entire period, to better describe the decay profile and estimate the total radiated energy accurately. We found that the flux profile can be well reproduced by using 8 power-law segments with a photon index of α_1, α_2, ..., and α_8, and with 7 breaks: T_{br1}, T_{br2}, ..., and T_{br7}, from earlier to later times. We described the initial flux rise until the second MAXI scan by two power-law segments. Because only 3 data points were available in this period, we fixed α_1, and α_2 at the values calculated from them and assumed T_{br1} and T_{br2} as the times of first and second MAXI scan. We note that this complex model is not physically motivated and is used just to obtain an accurate measurement of the fluence.

Figure 10 plots the light curve data and the best-fit model and Table 3 gives the best-fit parameters. We also estimated the X-ray fluence in 0.5–10 keV for the total outburst period as $F_{0.5-10\ \mathrm{keV}} = 2.9 \times 10^{-5}$ erg cm^2, by integrating the best-fit multiply broken power-law model in Fig. 10 over the entire period from $T = 0$ s to 3×10^7 s.

In Section 3.3.3, we found that including a partial covering absorption component give a better fit to the broadband X-ray spectrum at the early phase. To investigate if its inclusion affect the flux light curve, we tested to add `pcfabs` to the `TBabs*powerlaw` model and fit the soft X-ray spectra in Section 3.3.1. The `TBabs*pcfabs*powerlaw` model improved the fits of the spectra obtained by the end of the first rapid decay ($T < 10^5$ s) but not in the later period. The unabsorbed 0.5–10 keV fluxes were found to change only by $\lesssim 10\%$ from the `TBabs*powerlaw` model, and this does not affect the overall light curve profile in Fig. 10.
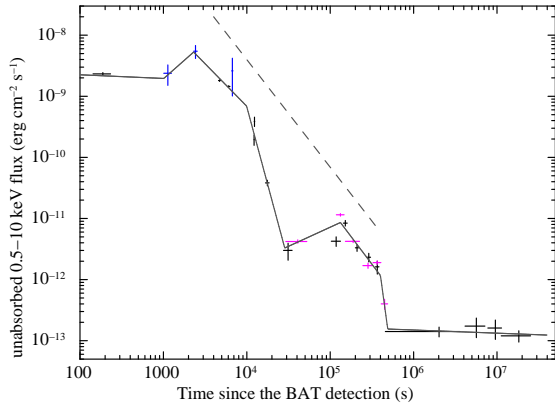
Figure 10. Flux light curve (same as Fig. 7a) and the best-fit multiply broken power-law model. The same data colors as Fig. 7(a) are adopted. The dashed line indicates a single power-law with an index of $\alpha = 1.7$ in terms of the time from the flux peak (see Equation 1).

Table 3. Best-fit parameters of the multiply broken power-law model for the long-term light curve.

Parameter	Unit	Value
α_1		0.06 (fixed)
T_{br1}	s	1.1×10^2 (fixed)
α_2		-1.2 (fixed)
T_{br2}	s	2.5×10^3 (fixed)
α_3		1.4 ± 0.1
T_{br3}	s	$(1.0 \pm 0.1) \times 10^4$
α_4		$5.1^{+0.8}_{-0.7}$
T_{br4}	s	$2.9^{+0.3}_{-0.2} \times 10^4$
α_5		-0.6 ± 0.1
T_{br5}	s	$(1.30 \pm 0.05) \times 10^5$
α_6		1.8 ± 0.2
T_{br6}	s	$> 3.8 \times 10^5$
α_7		> 6
T_{br7}	s	$4.8^{+0.5}_{-0.3} \times 10^5$
α_8		$0.1^{+0.2}_{-0.1}$
$F_{0.5-10keV}$ [a]	erg cm^{-2}	2.9×10^{-5}

[a] 0.5–10 keV fluence in the period of $T = 0–3 \times 10^7$ s.

4. DISCUSSION

4.1. *Summary of X-ray Properties*

We have studied the X-ray properties of Swift J0840.7−3516 using *Swift*, MAXI, NICER, and *NuSTAR* data. Here we summarise the results, to discuss the nature of the source in the following sections.

- A rapid outburst decay by ~ 5 orders of magnitude within ~ 5 days was observed. After the decay, the source flux was almost constant over 9 months (Fig. 1).

- The overall decay profile can be approximated with the function $\propto t^{-1.7}$, where t is the time from the flux peak. More precisely, the profile is better described with a multiply broken power-law model (Fig. 10 and Tab. 3). The total X-ray fluence until 3×10^7 s was estimated to be $\sim 3 \times 10^{-5}$ erg cm^{-2}.

- We detected strong short-term variations on time scales of $1–10^3$ s were seen during the decay (Fig. 3). A possible periodicity of 8.96 s was detected in the first *Swift*/XRT observation, but not in the other observations (Fig. 4 and Fig. 5).

- The soft X-ray spectrum was well described with an absorbed power-law model. The source showed the hardest spectrum with a photon index of ~ 1, which gradually increased with the decreasing flux and finally reached $\Gamma \sim 2$ after the decay (Fig. 7). The absorption column density was comparable to the total Galactic column, although some variations were present.

- A clear spectral rollover was observed at ~ 30 keV at the initial outburst rise. The wide-band X-ray spectrum at this phase was better described by adding a partial covering absorption or a (disk) blackbody component to an absorbed cutoff power-law model. An additional thermal component also improved the fit of the wide-band spectrum taken in the last period of the decay (Fig. 9 and Tab. 2).

- A possible absorption feature at ~ 3.4 keV was detected in $T \sim 2 \times 10^4$–5×10^4, when the light curve exhibited a plateau following the first steep decay (Fig. 6, 8, and Tab. 1). Assuming it as the neutral iron-K edge, the redshift is estimated to be $z = 1.1$.

4.2. *Possible Nature of the Source*
4.2.1. *A Galactic Origin*

Let us first investigate the possibility of a Galactic transient. Given that the source is located near the Galactic plane, it would be reasonable to take this possibility into account. Because the absorption column density is comparable to the total Galactic column for a large fraction of the outburst period, the source would not have a very close distance. Assuming an isotropic emission, the maximum and minimum luminosities in 0.5–10 keV are estimated as $2 \times$

$10^{37}(D/8 \text{ kpc})^2 \text{ erg s}^{-1}$ and $7 \times 10^{32}(D/8 \text{ kpc})^2 \text{ erg s}^{-1}$, respectively. The large luminosity range and the short time scale of the decay, and the relatively faint optical counterpart (with an apparent r' band magnitude of $\sim$ 20 mag; Mazaeva & IKI-FuN followFUp Collaboration 2020) rule out the possibility of a high mass X-ray binary (e.g., Walter et al. 2015). The timescale of the X-ray decay is much shorter than magnetar outbursts (~ 100 days; Coti Zelati et al. 2018), although a couple of them showed two-step decays reminiscent of that seen in our target. The observed hard, non-thermal spectrum without any prominent emission lines also makes unlikely the possibilities of a stellar flare (Güdel & Nazé 2009) and a CV (Mukai 2017).

We have confirmed the 8.96-s peak reported by Kennea et al. (2020) in the periodogram made with the first $Swift$/XRT observation. Given the fact that it did not appear in any other observations, the variation was either a transient phenomenon of the source or an artefact (such as red noise). If the former is the case, it is difficult, due to the limited exposure, to determine whether it is a pulsation or a quasi-periodic oscillation (QPO). Hence, the possibilities of an X-ray binary pulsar and a magnetar are not proved nor ruled out.

Typical black hole (BH) and neutron star (NS) low mass X-ray binaries (LMXBs) are also difficult to explain some of the observed properties of Swift J0840.7−3516. The luminosity range of the decay is consistent with LMXBs, and the upper limit of the radio flux, 18 μJy at 7.5 Hz, obtained 5 days after the discovery (Borghese et al. 2020), also agrees with the radio/X-ray flux correlations of both BH and NS LMXBs (e.g., Corbel et al. 2013). However, the observed decay period of ~ 5 days is much shorter than those of typical LMXBs: a few tens of days to more than a year. This means that Swift J0840.7−3516 accreted much smaller mass than normal LMXBs in an unusually short period. Moreover, the spectrum in the outburst rise had a somewhat small photon index, $\Gamma \sim 1.0$, compared with typical LMXBs in the hard state, $\Gamma \sim 1.5$–1.9 (e.g., Done et al. 2007).

Yet these unusual properties cannot completely rule out a LMXB nature. There are actually some LMXBs that show similar properties. An LMXB candidate showing such a short outburst with a similar luminosity range has recently been found (MAXI J1957+032; Beri et al. 2019). There are also several known LMXBs with short outbursts but smaller peak luminosities of 10^{34}–$10^{36} \text{ erg s}^{-1}$, which are called "very faint X-ray transient" (VFXT; Wijnands et al. 2006; Degenaar & Wijnands 2010; Bahramian et al. 2020). In addition, very hard spectra in bright hard state have been observed in a couple of NS LMXBs (Parikh et al. 2017) and BH LMXBs including V 404 Cyg (e.g., Kimura et al. 2016), V4641 Sgr (e.g., Maitra & Bailyn 2006), and Swift J1858.6−0814 (Hare et al. 2020). All these sources have a strong short-term flux variation by a more than order of magnitude (e.g., Kitamoto et al. 1989; Revnivtsev et al. 2002; Wijnands et al. 2017), also in agreement with the present case. In addition, partial covering absorption is sometimes required in these sources especially at high flux phases (Kimura et al. 2016), consistent with Swift J0840.7−3516 at a bright phase.

We note that the photon index of Swift J0840.7−3516 after the decay, $\lesssim 2$ is reminiscent of a BH rather than a NS LMXB, which usually shows a larger value, $\Gamma \sim 3$ (Wijnands et al. 2015), although the NS LMXB EXO 1745−248 showed a similar hard spectrum in quiescence (Rivera Sandoval et al. 2018). On the other hand, a NS LMXB would rather be favored, in that a very small radius of the thermal component, 1–2 (D/8 kpc) km, consistent with emission from a NS surface, was obtained from the $NuSTAR$+$Swift$/XRT+NICER spectrum at a faint phase. This holds even if the observed power-law component was entirely produced by Comptonized disk photons. Assuming conservation of the number of photons and an isotropic scattered emission (Kubota & Makishima 2004), and using the intrinsic disk photons estimated from the best-fit `diskbb+cutoffpl` model, we obtain the inner disk radius as ~ 3 (D/8 kpc) km (where $i = 60°$ is assumed). Similar thermal emission likely emitted by the NS surface can be seen in NS LMXBs at low X-ray luminosities below $\sim 10^{35} \text{ erg s}^{-1}$ but not at a more luminous hard state, where the power-law component dominates the X-ray flux (e.g., Sakurai et al. 2014; Shidatsu et al. 2017). The thermal component in Swift J0840.7−3516 was observed at a consistent luminosity; the second rapid decay from 10^5 s since the discovery, in which this component was found, started at $\sim 10^{35} (D/8 \text{ kpc})^2 \text{ erg s}^{-1}$.

Even if an LMXB scenario works for all the properties raised above, the observed absorption feature is difficult to explain. Although ionized Si and S lines from disk winds are sometimes seen at similar energies (e.g., Ueda et al. 2009), they are much weaker than the present case and always with strong iron K α lines at ~ 7 keV. Assuming the observed feature as the redshifted Fe K edge, we obtained $z = 1.1$. If this is the gravitational redshift caused by a Schwarzschild stellar mass BH, the feature should be produced at $\sim 1.3 R_{\rm S}$, where $R_{\rm S}$ is the Schwarzschild radius. It is unclear that an absorber with such a small size can exist in the vicinity of a BH.

Another possibility is that the observed feature is a different blueshifted line produced by a relativistic outflow in an relativistic speed, like baryonic jets observed in SS 433. However, it is unclear if such baryonic jets can exist at a low Eddington ratio and produce a single absorption feature.

Instead, the origin of the source might be explained by a tidal disruption of an asteroid by a neutron star (Newman & Cox 1980; Colgate & Petschek 1981), which was considered for the origin of GRBs 30–40 years ago. In this model, the collision of an asteroid and a NS surface produces strong MeV gamma-rays and hot plasma. The plasma could be rapidly cooled by radiation and cause Compton down scattering, resulting in a power-law shaped X-ray spectrum. The radiation energy of Swift J0840.7−3516 released in 10^7 s is estimated as $2 \times 10^{39}(D/8 \text{ kpc})^2$ erg, which is converted to a total accreted mass of $\sim 10^{20}$ $(\eta/0.01)$ $(D/8 \text{ kpc})^2$ g (where η is the radiative efficiency), consistent with an asteroid. It is unclear, however, whether or not this scenario can explain the observed evolution of photon index of the X-ray spectrum and the absorption feature.

4.2.2. An Extragalactic Origin

We next investigate the possibility of an extragalactic origin. If the source is an extragalactic X-ray binary located in a nearby galaxy, the maximum luminosity is far beyond the Eddington luminosity of a BH with a mass of 10 $M_\odot$. Even if the distance is as small as ~ 1 Mpc, the peak luminosity is calculated as $\gtrsim 10^{41}$ erg s^{-1}. Such a bright X-ray binary is categorized as a hyper luminous X-ray source and considered to have an intermediate mass BH (Farrell et al. 2009). In this case, it is even more difficult, than in the case of a normal X-ray binary with a stellar mass BH, to explain the short duration of the outburst, because of the large accretion disk size. For the same reason, an AGN origin is unlikely.

Some of the observed properties of Swift J0840.7−3516 agree with those of GRBs. Absorption features have been detected in a few GRBs (Amati et al. 2000; Frontera et al. 2004; Bellm et al. 2014) and interpreted as the redshifted iron K line or edge, although they were detected mainly in the prompt phase, unlike the present case (but see Bellm et al. 2014). The absorption feature in our case was observed just after the first rapid decay, which may be considered to be the beginning of the afterglow, and could be explained by the interaction between the jets and the surrounding gas. If the estimated redshift $z = 1.1$ is the cosmological redshift, it is converted to a luminosity distance of 7 Gpc, assuming $H_0 = 70$ km s^{-1} Mpc^{-1}, $\Omega_M = 0.3$, and $\Omega_\Lambda = 0.7$. In this case, the maximum and min-

imum luminosities are calculated to be 1×10^{49} erg s^{-1} and 4×10^{44} erg s^{-1}, respectively, where isotropic emission is assumed. The redshift and maximum luminosity are well within the distribution of known GRBs. The source showed a hard spectrum with $\Gamma \sim 1$ and a spectral rollover at ~ 30 keV in the early phase, which are compatible with soft GRBs in the prompt phase (e.g., Yonetoku et al. 2010). Using the best-fit cutoff power-law model of the Swift/XRT+BAT spectrum (see Section 3.3.3), we obtain the 2–10 keV luminosity of 5×10^{48} erg s^{-1} in the rest frame of the source. This is consistent with the correlation between the peak energy and X-ray luminosity of Swift-detected GRBs reported by D'Avanzo et al. (2012).

The decay profile for the first 10^6 s and the spectral evolution of Swift J0840.7−3516 also share similar properties with GRBs. The two-step decay could be attributed to the prompt and afterglow emission. However, the observed plateau phase started later and lasted longer by one order of magnitude than the typical shallow decay phase of GRBs (Zhang et al. 2006). Moreover, the constant flux over 9 months after the decay is very different from, and difficult to explain by, X-ray afterglows of GRBs.

Instead, the source may be interpreted as a TDE by a supermassive BH. The overall decay profile is approximated to $t^{-1.7}$, which is consistent with what is theoretically expected for a TDE ($t^{-5/3}$; Rees 1988; Phinney 1989) and the actual X-ray light curves of observed TDEs (e.g., Burrows et al. 2011; Cenko et al. 2012). The strong short-term variability is reminiscent of the jetted TDE Swift J164449.3+573451 (Burrows et al. 2011; Mangano et al. 2016, hereafter Swift J1644). X-ray Absorption features have also been detected in a TDE at lower energies than that in the present case (Miller et al. 2015), and were interpreted as an outflow at a velocity of a few hundred km s^{-1}. The total radiation energy in 1–20 keV is calculated from the fluence to be 9×10^{52} erg in the rest frame of Swift J0840.7−3516, assuming an isotropic emission and a luminosity distance of 7 Gpc. This corresponds to a total accreted mass of ~ 0.9 $M_\odot$, assuming the radiative efficiency of the standard accretion disk of a Schwarzschild BH. The peak luminosity, $\sim 10^{49}$ erg s^{-1} is more than one order of magnitude larger than that of the most luminous TDE Swift J1644.

Swift J1644 exhibited a steep flux drop ~ 500 days after the discovery and an almost constant flux for the following ~ 1000 days, which can be explained by the end of accretion and scattering of X-rays with the surrounding gas, respectively (Cheng et al. 2016). Similar flux behaviors were observed in Swift J0840.7−3516,

with a rapid decay until $T \sim 5 \times 10^5$ s and a following constant-flux phase. If the end of the decay at $\sim 5 \times 10^5$ s actually reflects the end of accretion, the BH mass ($M_{\rm BH}$) of Swift J0840.7−3516 can be estimated by comparing the decay time, or the accretion period, of the two sources, as described below. We note that the scattering echo scenario for the constant-flux phase requires spectral softening, because of the energy dependence of the scattering angle. However, no significant softening was observed and therefore a different explanation would be needed in the present case.

When a star is tidally disrupted by a BH, some of the disrupted matter orbits around it and falls onto the BH (Rees 1988). The kinetic energy of the disrupted matter in the unit mass is described as

$$\epsilon \sim \frac{GM_{\rm BH}}{a}, \qquad (2)$$

where a and G are the semi major axis and the Gravitational constant, respectively. Combining the Kepler's third law, $T \sim \sqrt{a^3/GM_{\rm BH}}$, we obtain

$$T \propto M_{\rm BH}\epsilon^{-\frac{3}{2}}. \qquad (3)$$

Thus, the accretion time is proportional to $M_{\rm BH}$.

Using this relation, the BH mass of Swift J0840.7−3516 should be $\sim 10^2$ times smaller than that of Swift J1644, which was previously estimated as 10^6–10^7 $M_\odot$ (Burrows et al. 2011). In this case, we obtain a BH mass of Swift J0840.7−3516 of 10^4–10^5 $M_\odot$, and therefore we may have witnessed a rare case of a TDE in a dwarf galaxy. The smaller BH mass and higher peak luminosity than those of Swift J1644 imply that Swift J0840.7−3516 is a more highly beamed, jetted TDE. This is of course just a rough estimate, and different approaches such as observations of the host galaxy would be required for a more accurate measurement.

A QPO at 5 mHz was detected in Swift J1644 and associated with the Keplerian frequency at the innermost stable circular orbit of the BH (Reis et al. 2012). If the observed 8.96 s variation in Swift J0840.7−3516 is explained by a QPO produced in the same manner, its BH mass is calculated to be $10^4 - 10^5 M_\odot$, depending on the BH spin. This is consistent with the mass estimated above from the decay period.

5. SUMMARY AND FUTURE PROSPECTS

Using X-ray data from MAXI, *Swift*, NICER, and *NuSTAR*, we have found unusual X-ray properties of Swift J0840.7−3516 that are difficult to explain by any

of known class of objects. A plausible interpretation may be an LMXB with multiple extreme properties, or a tidal disruption of a star by a supermassive BH or an asteroid by a Galactic NS. In any case, this source has provided an opportunity to study an interesting and perhaps rare astrophysical phenomena around a compact object.

To uncover the true nature of the source, observations of the optical/infrared counterpart are essential. So far, only several results from photometric observations have been reported, all of which were performed in the first couple of days after the discovery. Future high sensitivity and spatial resolution optical imaging, using largest class telescopes, could provide morphology information of the optical counterpart and determine its host galaxy if it is an extragalactic object. In addition, high sensitivity spectroscopy would enable an accurate determination of the redshift of the source.

REFERENCES

Amati, L., Frontera, F., Vietri, M., et al. 2000, Science,
   290, 953, doi: 10.1126/science.290.5493.953

Arnaud, K. A. 1996, in Astronomical Society of the Pacific
   Conference Series, Vol. 101, Astronomical Data Analysis
   Software and Systems V, ed. G. H. Jacoby & J. Barnes,
   17

Bahramian, A., Heinke, C. O., Kennea, J. A., et al. 2020,
   MNRAS, submitted, arXiv:2009.10322.
   https://arxiv.org/abs/2009.10322

Bellm, E. C., Barrière, N. M., Bhalerao, V., et al. 2014,
   ApJL, 784, L19, doi: 10.1088/2041-8205/784/2/L19

Beri, A., Altamirano, D., Wijnands, R., et al. 2019,
   MNRAS, 486, 1620, doi: 10.1093/mnras/stz938

Borghese, A., Zelati, F. C., Rea, N., et al. 2020, The
   Astronomer's Telegram, 13472

Buccheri, R., Bennett, K., Bignami, G. F., et al. 1983,
   A&A, 128, 245

Burrows, D. N., Kennea, J. A., Ghisellini, G., et al. 2011,
   Nature, 476, 421, doi: 10.1038/nature10374

Cash, W. 1979, ApJ, 228, 939, doi: 10.1086/156922

Cenko, S. B., Krimm, H. A., Horesh, A., et al. 2012, ApJ,
   753, 77, doi: 10.1088/0004-637X/753/1/77

Cheng, K. S., Chernyshov, D. O., Dogiel, V. A., Kong, A.
   K. H., & Ko, C. M. 2016, ApJL, 816, L10,
   doi: 10.3847/2041-8205/816/1/L10

Colgate, S. A., & Petschek, A. G. 1981, ApJ, 248, 771,
   doi: 10.1086/159201

Corbel, S., Coriat, M., Brocksopp, C., et al. 2013, MNRAS,
   428, 2500, doi: 10.1093/mnras/sts215

Coti Zelati, F., Rea, N., Pons, J. A., Campana, S., &
   Esposito, P. 2018, MNRAS, 474, 961,
   doi: 10.1093/mnras/stx2679

D'Avanzo, P., Salvaterra, R., Sbarufatti, B., et al. 2012,
   MNRAS, 425, 506, doi: 10.1111/j.1365-2966.2012.21489.x

Degenaar, N., & Wijnands, R. 2010, A&A, 524, A69,
   doi: 10.1051/0004-6361/201015322

Done, C., Gierliński, M., & Kubota, A. 2007, A&A Rv, 15,
   1, doi: 10.1007/s00159-007-0006-1

Evans, P. A., Tohuvavohu, A., & Neil Gehrels Swift
   Observatory Team. 2020, GRB Coordinates Network,
   26982

Evans, P. A., Beardmore, A. P., Page, K. L., et al. 2007,
   A&A, 469, 379, doi: 10.1051/0004-6361:20077530

—. 2009, MNRAS, 397, 1177,
   doi: 10.1111/j.1365-2966.2009.14913.x

Farrell, S. A., Webb, N. A., Barret, D., Godet, O., &
   Rodrigues, J. M. 2009, Nature, 460, 73,
   doi: 10.1038/nature08083

Frontera, F., Amati, L., in 't Zand, J. J. M., et al. 2004,
   ApJ, 616, 1078, doi: 10.1086/425066

Gehrels, N., Chincarini, G., Giommi, P., et al. 2004, ApJ,
   611, 1005, doi: 10.1086/422091

Gendreau, K. C., Arzoumanian, Z., Adkins, P. W., et al.
   2016, in Society of Photo-Optical Instrumentation
   Engineers (SPIE) Conference Series, Vol. 9905, Space
   Telescopes and Instrumentation 2016: Ultraviolet to
   Gamma Ray, ed. J.-W. A. den Herder, T. Takahashi, &
   M. Bautz, 99051H, doi: 10.1117/12.2231304

Güdel, M., & Nazé, Y. 2009, A&A Rv, 17, 309,
   doi: 10.1007/s00159-009-0022-4

Hare, J., Tomsick, J. A., Buisson, D. J. K., et al. 2020,
   ApJ, 890, 57, doi: 10.3847/1538-4357/ab6a12

Harrison, F. A., Craig, W. W., Christensen, F. E., et al.
   2013, ApJ, 770, 103, doi: 10.1088/0004-637X/770/2/103

HEASARC. 2014, HEAsoft: Unified Release of FTOOLS
   and XANADU, Astrophysics Source Code Library.
   http://ascl.net/1408.004

Iwakiri, W., Gendreau, K., Enoto, T., et al. 2020, The
   Astronomer's Telegram, 13456

Kennea, J. A., Palmer, D. M., Siegel, M. H., et al. 2020,
   The Astronomer's Telegram, 13452

Kimura, M., Isogai, K., Kato, T., et al. 2016, Nature, 529,
   54, doi: 10.1038/nature16452

Kitamoto, S., Tsunemi, H., Miyamoto, S., Yamashita, K.,
   & Mizobuchi, S. 1989, Nature, 342, 518,
   doi: 10.1038/342518a0

Kubota, A., & Makishima, K. 2004, ApJ, 601, 428,
   doi: 10.1086/380433

Lewin, W. H. G., van Paradijs, J., & Taam, R. E. 1993,
   SSRv, 62, 223, doi: 10.1007/BF00196124

Lipunov, V., Gorbovskoy, E., Tiurina, N., et al. 2020, GRB
   Coordinates Network, 26984

Maitra, D., & Bailyn, C. D. 2006, ApJ, 637, 992,
   doi: 10.1086/498422

Malesani, D. B., Izzo, L., Palmerio, J., et al. 2020, GRB
   Coordinates Network, 26989

Mangano, V., Burrows, D. N., Sbarufatti, B., & Cannizzo,
   J. K. 2016, ApJ, 817, 103,
   doi: 10.3847/0004-637X/817/2/103

Matsuoka, M., Kawasaki, K., Ueno, S., et al. 2009, PASJ,
   61, 999, doi: 10.1093/pasj/61.5.999

Mazaeva, E., & IKI-FuN followFUp Collaboration. 2020,
   GRB Coordinates Network, 27003

Melandri, A., Covino, S., Fugazza, D., D'Avanzo, P. I., &
   REM Team. 2020, GRB Coordinates Network, 26986

Miller, J. M., Kaastra, J. S., Miller, M. C., et al. 2015,
   Nature, 526, 542, doi: 10.1038/nature15708

Mitsuda, K., Inoue, H., Koyama, K., et al. 1984, PASJ, 36, 741

Mukai, K. 1993, Legacy, 3, 21. https://heasarc.gsfc.nasa.gov/docs/journal/pimms3.html

—. 2017, PASP, 129, 062001, doi: 10.1088/1538-3873/aa6736

Nandra, K., O'Neill, P. M., George, I. M., & Reeves, J. N. 2007, MNRAS, 382, 194, doi: 10.1111/j.1365-2966.2007.12331.x

Negoro, H., Kohama, M., Serino, M., et al. 2016, PASJ, 68, S1, doi: 10.1093/pasj/psw016

Newman, M. J., & Cox, A. N. 1980, ApJ, 242, 319, doi: 10.1086/158465

Niwano, M., Mihara, T., Nakajima, M., et al. 2020, GRB Coordinates Network, 26987

Osborne, J. P., Beardmore, A. P., Evans, P. A., Goad, M. R., & Swift-XRT Team. 2020, GRB Coordinates Network, 26996

Parikh, A. S., Wijnands, R., Degenaar, N., et al. 2017, MNRAS, 468, 3979, doi: 10.1093/mnras/stx747

Phinney, E. S. 1989, in IAU Symposium, Vol. 136, The Center of the Galaxy, ed. M. Morris, 543

Rees, M. J. 1988, Nature, 333, 523, doi: 10.1038/333523a0

Reis, R. C., Miller, J. M., Reynolds, M. T., et al. 2012, Science, 337, 949, doi: 10.1126/science.1223940

Revnivtsev, M., Gilfanov, M., Churazov, E., & Sunyaev, R. 2002, A&A, 391, 1013, doi: 10.1051/0004-6361:20020865

Rivera Sandoval, L. E., Wijnands, R., Degenaar, N., et al. 2018, MNRAS, 479, 2777, doi: 10.1093/mnras/sty1535

Sakurai, S., Torii, S., Noda, H., et al. 2014, PASJ, 66, 10, doi: 10.1093/pasj/pst010

Shidatsu, M., Tachibana, Y., Yoshii, T., et al. 2017, ApJ, 850, 155, doi: 10.3847/1538-4357/aa93f0

Ueda, Y., Yamaoka, K., & Remillard, R. 2009, ApJ, 695, 888, doi: 10.1088/0004-637X/695/2/888

Walter, R., Lutovinov, A. A., Bozzo, E., & Tsygankov, S. S. 2015, A&A Rv, 23, 2, doi: 10.1007/s00159-015-0082-6

Wijnands, R., Degenaar, N., Armas Padilla, M., et al. 2015, MNRAS, 454, 1371, doi: 10.1093/mnras/stv1974

Wijnands, R., Parikh, A. S., Altamirano, D., Homan, J., & Degenaar, N. 2017, MNRAS, 472, 559, doi: 10.1093/mnras/stx2006

Wijnands, R., in 't Zand, J. J. M., Rupen, M., et al. 2006, A&A, 449, 1117, doi: 10.1051/0004-6361:20054129

Wilms, J., Allen, A., & McCray, R. 2000, ApJ, 542, 914, doi: 10.1086/317016

Yonetoku, D., Murakami, T., Tsutsui, R., et al. 2010, PASJ, 62, 1495, doi: 10.1093/pasj/62.6.1495

Zhang, B., Fan, Y. Z., Dyks, J., et al. 2006, ApJ, 642, 354, doi: 10.1086/500723